Eur. Phys. J. A (2016) **52**: 65
DOI 10.1140/epja/i2016-16065-6

The European Physical Journal A

Review

Hyperon puzzle, hadron-quark crossover and massive neutron stars[⋆]

Kota Masuda[1,2,a], Tetsuo Hatsuda[2,3], and Tatsuyuki Takatsuka[2]

[1] Department of Physics, The University of Tokyo, Tokyo 113-0033, Japan
[2] Theoretical Research Division, Nishina Center, RIKEN, Wako 351-0198, Japan
[3] Kavli IPMU (WPI), The University of Tokyo, Chiba 277-8583, Japan

Received: 19 August 2015 / Revised: 5 March 2016

Communicated by D. Blaschke

Abstract. Bulk properties of cold and hot neutron stars are studied on the basis of the hadron-quark crossover picture where a smooth transition from the hadronic phase to the quark phase takes place at finite baryon density. By using a phenomenological equation of state (EOS) "CRover", which interpolates the two phases at around 3 times the nuclear matter density (ρ_0), it is found that the cold NSs with the gravitational mass larger than $2M_\odot$ can be sustained. This is in sharp contrast to the case of the first-order hadron-quark transition. The radii of the cold NSs with the CRover EOS are in the narrow range (12.5 ± 0.5) km which is insensitive to the NS masses. Due to the stiffening of the EOS induced by the hadron-quark crossover, the central density of the NSs is at most $4\rho_0$ and the hyperon-mixing barely occurs inside the NS core. This constitutes a solution of the long-standing hyperon puzzle. The effect of color superconductivity (CSC) on the NS structures is also examined with the hadron-quark crossover. For the typical strength of the diquark attraction, a slight softening of the EOS due to two-flavor CSC (2SC) takes place and the maximum mass is reduced by about $0.2M_\odot$. The CRover EOS is generalized to the supernova matter at finite temperature to describe the hot NSs at birth. The hadron-quark crossover is found to decrease the central temperature of the hot NSs under isentropic condition. The gravitational energy release and the spin-up rate during the contraction from the hot NS to the cold NS are also estimated.

1 Introduction

Strongly interacting matter described by quantum chromodynamics (QCD) is believed to have a rich phase structure under the change of external parameters such as the temperature (T) and the baryon chemical potential (μ) [1]. At low T and μ, the system is in the hadronic phase where the dynamical breaking of chiral symmetry and confinement of quarks and gluons take place. At high T and low μ, the quark-gluon plasma with deconfined quarks and gluons was predicted theoretically and is under active experimental studies by the relativistic heavy-ion collisions at RHIC and LHC [2]. At low T and high μ, the superconducting quark matter with deconfined quarks is expected to appear, which is relevant to the central core of neutron stars [3].

The transition from the hadronic matter to the quark-gluon plasma at high T has been studied quantitatively by using the lattice QCD simulations [4]. On the other hand, the transition from the hadronic matter to the quark matter at high μ is not well understood partly due to the lack of reliable first-principle theoretical methods; the Monte Carlo simulations in lattice QCD are not suitable for $\mu/T \gg 1$ because of the fermion sign problem [1].

Under such circumstance, any information from neutron stars (NSs), whose central cores may reach the baryon density relevant to the hadron-quark transition, is quite useful to understand the structure of high density matter. Among various observables for NSs [5], the surface temperature (T_s) the mass (M), the radius (R) and the magnetic field (B) are particularly informative. Indeed, a massive NS (PSR J1614-2230) with $M = (1.97 \pm 0.04)M_\odot$ observed through the Shapiro delay technique [6] and another massive NS (PSR J0348+0432) with $M = (2.01 \pm 0.04)M_\odot$ [7] may give stringent constraints on the equation of state (EOS) of dense matter.

Historically, Gibbs phase equilibrium conditions have been adopted to describe the transition between the hadronic matter composed of point-like hadrons and the quark matter composed of weakly interacting quarks. However, in the transition region, neither the assumption

---

[⋆] Contribution to the Topical Issue on "Exotic matter in neutron stars" edited by David Blaschke, Jürgen Schaffner-Bielich, Hans-Josef Schulze.

[a] e-mail: `masuda@nt.phys.s.u-tokyo.ac.jp`

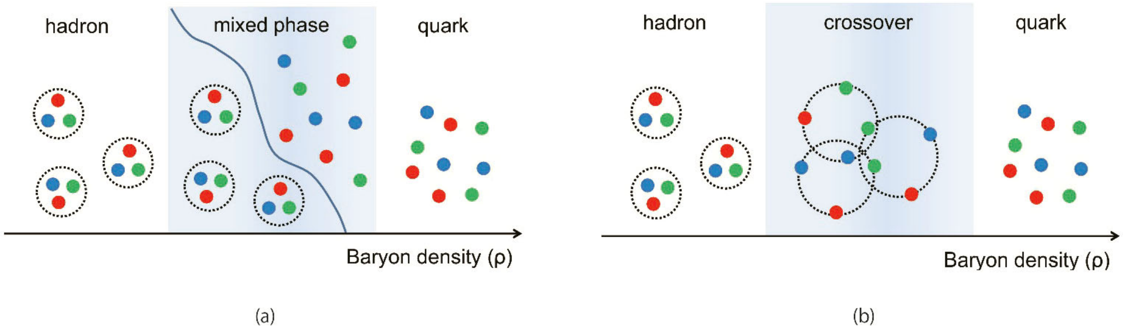

Fig. 1. Schematic pictures of the QCD phases as a function of the baryon density (ρ) under the assumption of (a) the first-order transition and (b) the hadron-quark crossover. The mixed-phase region in (a) and the crossover region in (b) are indicated by the shaded area.

of point-like hadrons nor that of weakly interacting quarks are justified. Indeed, there may arise a smooth crossover between the hadronic matter and the quark matter: Furthermore, the system in the crossover region would be strongly interacting [8].

Figure 1 illustrates the difference between (a) the first-order transition where the phase separation between hadrons and quarks takes place, and (b) the crossover where the percolation of finite size hadrons takes place. Such a percolation picture of hadrons has been first discussed in refs. [9,10], and later elaborated in the contexts of the hadron-quark continuity [11,12] and the hadron-quark crossover [13,14].

Recently, the present authors have shown that the hadron-quark crossover at around three times the normal nuclear matter density ($\rho_0 = 0.17\,\mathrm{fm}^{-3}$) can lead to a stiffening of EOS and sustain the $2M_\odot$ NSs [15–17] in contrast to the case of hadron-quark first-order transition. Also, it was shown that such a stiffening due to hadron-quark crossover can avoid the so-called "Hyperon Puzzle" as discussed in sect. 2. (See also the related works [18–20].)

In this article, we discuss bulk properties of cold and hot NSs on the basis of the new EOS with the hadron-quark crossover (the "CRover" EOS) introduced in [15–17]. In sect. 2, we summarize the conventional hadronic EOS with and without hyperons. In sect. 3, we summarize detailed properties of hadronic EOS to be used throughout the present study. In sect. 4, we summarize the quark EOS based on the (2+1)-flavor Nambu–Jona-Lasinio (NJL) model at high density. In sect. 5, We introduce a phenomenological approach to interpolate the hadronic matter and the quark matter. In sect. 6, we show the bulk properties of cold neutron stars using the CRover EOS at $T = 0$ (abbreviated as cold CRover EOS) with and without color superconductivity. In sect. 7, we show the bulk properties of hot neutron stars at birth using CRover EOS at $T \neq 0$ (abbreviated as hot CRover EOS). Section 8 is devoted to summary and concluding remarks.

2 Hyperon Puzzle

Let us first consider what would be the neutron star structure under the hadronic EOS with and without hyperons ($Y{=}\Lambda$, Σ^-, Ξ^-). Although there exist large uncertainties for the two-body Y-N interactions[1], various different models suggest that hyperons may appear at densities of several times ρ_0. Those hyperons introduce significant softening of EOS and even the well-established $1.4M_\odot$ NSs may not be reproduced (see the reviews, [25,26] and the references therein). The three-body force in the hyperon sector originally suggested in [27,28] may or may not describe the $2M_\odot$ NSs depending on its strength [25,29–32]. This is called the "Hyperon Puzzle".

To see the "Hyperon Puzzle" more explicitly, let us take four hadronic EOS with hyperons, TNI2u, TNI2, AV18+TBF+$\Lambda\Sigma$, and SCL3$\Lambda\Sigma$. Here TNI2u (TNI2) is the EOS based on the non-relativistic G-matrix approach with the incompressibility $\kappa = 250\,\mathrm{MeV}$ and with (without) the hyperon three-body force. AV18+TBF+$\Lambda\Sigma$ [33] is also based on the non-relativistic G-matrix approach with the AV18 nucleon-nucleon potential, the Urbana-type three-body nucleon potential and the Nijmegen soft-core nucleon-hyperon potential. SCL3$\Lambda\Sigma$ [34] is a relativistic mean-field model with chiral SU(3) symmetry. As a typical nuclear EOS without the hyperons, we take APR [35].

In fig. 2(a), we plot the hadronic EOS with hyperons (TNI2u, TNI2, AV18+TBF+$\Lambda\Sigma$ and SCL3$\Lambda\Sigma$) together with APR. Filled circles on each line denote the density where the hyperon-mixing starts to occur. One can see that i) the mixture of hyperons softens the equation of state relative to APR, and ii) onset of the hyperon-mixing is shifted to higher density if we consider the three-body interaction in the hyperon sector. In fig. 2(b), the M-R relations with these EOSs are plotted by the same color lines. The gray band shows $M = (1.97 \pm 0.04)M_\odot$ corresponding to PSR J1614-2230 [6] and the solid horizontal line shows $M = 1.44M_\odot$ corresponding to PSR 1913+16. In table 1, we summarize the nuclear incompressibility κ, the threshold density for Λ and Σ^-, the maximum mass M_{max}, the radius and the central density ρ_c for these hadronic EOSs with hyperons. EOSs become soft drastically due to the emergence of hyperons.

---

[1] We note that it is important to have new data on hyperon interactions from the Y-N scattering and hypernuclei experiments at J-PARC [21–23] and also from the lattice QCD simulations at the physical quark masses [24].

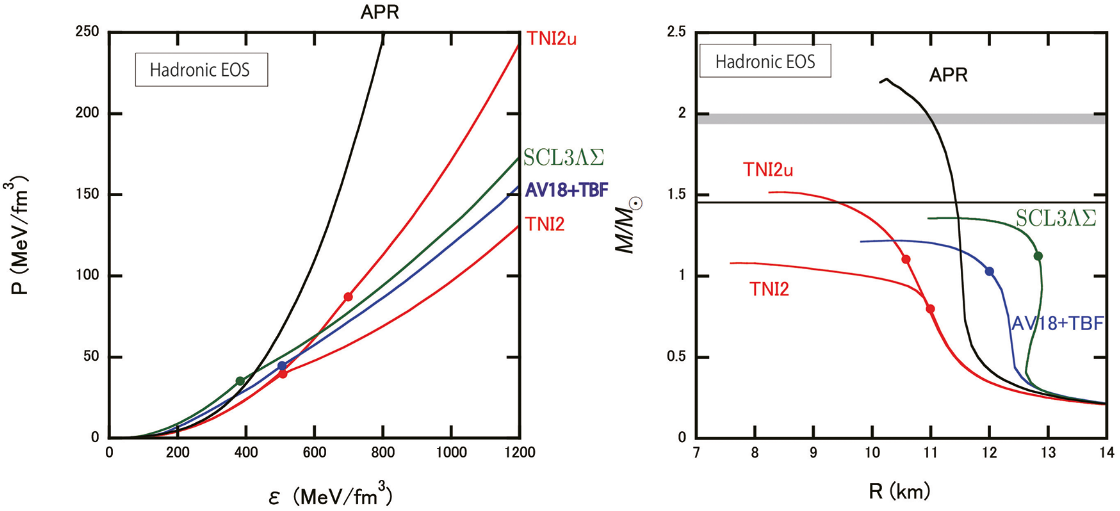

(a)

(b)

Fig. 2. (a) The hadronic equation of states with and without the hyperon mixing. The black line denotes the EOS without hyperon, APR (AV18+δv+ UIX*). The red lines correspond to the EOS with hyperons; TNI2 (only three-nucleon force with $\kappa = 250\,\text{MeV}$) and TNI2u (universal three-baryon force with $\kappa = 250\,\text{MeV}$). The blue line corresponds to AV18+TBF+$\Lambda\Sigma$ (G-matrix with AV18 + 3-nucleon force + hyperons), and the green line corresponds to SCL3$\Lambda\Sigma$ (relativistic mean-field model with chiral SU(3) symmetry). (b) M-R relations for five EOSs considered in (a). In both figures, filled circles on each line show the density where the hyperons start to mix. Also, the gray band denotes $M = (1.97 \pm 0.04)M_\odot$ for PSR J1614-2230 [6] and the solid horizontal line shows $M = 1.44M_\odot$ corresponding to PSR 1913+16. Those figures are adapted and modified from [15,16].

3 Hadronic EOS with Hyperons

Since we will take TNI2u and TNI2 in the following analyses, we summarize here how these hadronic EOS with hyperons are obtained[2] [27,28,36]:

1) Effective two-baryon potentials $\tilde{V}_{BB'}$ ($B = n$, p, Λ, Σ^-) are constructed on the basis of the G-matrix formalism to take into account their density dependence.
2) A phenomenological thee-nucleon interaction expressed in a form of two-body potential $\tilde{U}_{NN'}$ [37] is introduced to reproduce the saturation of symmetric nuclear matter (the saturation density $\rho_0 = 0.17\,\text{fm}^{-3}$ and the binding energy $E_0 = -16\,\text{MeV}$) and the incompressibility $\kappa = 250\,\text{MeV}$ compatible with experiments.
3) Universal three-body repulsion is assumed for the hyperons in TNI2u through the replacement, $\tilde{U}_{NN'} \to \tilde{U}_{BB'}$, which is necessary to sustain $1.4M_\odot$ even with hyperons, while the three-body repulsion is introduced only in the nucleon sector in TNI2.
4) By using $\tilde{V}_{BB'} + \tilde{U}_{BB'}$, we calculate the particle composition y_i ($i = n$, p, Λ, Σ^-, e^- and μ^-) under charge neutrality and β-equilibrium to obtain the hadronic EOS as a function of total baryon density ρ at $T = 0$.

Table 1. Properties of various hadronic EOSs with hyperons; TNI2, TNI2u, AV18+TBF+$\Lambda\Sigma$ and SCL3$\Lambda\Sigma$. κ is the nuclear incompressibility and ρ_{th} is the threshold density of hyperon-mixing with ρ_0 being the normal nuclear density. R and ρ_c denote the radius and central density of the maximum mass ($M_{\max}$) NS, respectively. The numbers in the parentheses are those without hyperons. "*"s indicate that the numbers are read from the figures in [33].

EOS	TNI2	TNI2u	AV18+TBF	SCL3$\Lambda\Sigma$
κ (MeV)	250	250	192	211
$\rho_{\text{th}}(\Lambda)/\rho_0$	2.95	4.01	2.8*	2.24
$\rho_{\text{th}}(\Sigma^-)/\rho_0$	2.83	4.06	1.8*	2.24
$M_{\max}/M_\odot$	1.08	1.52	1.22	1.36
	(1.62)		(2.00)	(1.65)
R(km)	7.70	8.43	10.46	11.42
	(8.64)		(10.54)	(10.79)
ρ_c/ρ_0	16.10	11.06	7.35	6.09
	(9.97)		(6.53)	(6.85)

As shown in fig. 2(a), TNI2u EOS is moderately stiff even with hyperon-mixing, but the corresponding maximum mass of NS is $1.5M_\odot$, so that it is not sufficient to reproduce $2M_\odot$ NSs as shown in fig. 2(b).

---

[2] "TNI" implies that the Three-Nucleon Interaction is taken into account, "2" implies $\kappa = 250\,\text{MeV}$, and "u" implies that the three-body interaction is introduced universally in the octet baryon sector.

4 (2+1)-flavor quark EOS with color superconductivity

At high baryon density relevant to the central core of the NSs, baryons are started to overlap with each other and quark degrees of freedom may arise with $\mu \sim$ 400–500 MeV. However, at such chemical potentials, the QCD running coupling is still large and the quark matter would be strongly interacting. Analogous strongly interacting matter at finite T was originally discussed theoretically in [38–40] and was later studied experimentally in the relativistic heavy-ion collisions at RHIC and LHC [2].

Under the situation that the Monte Carlo simulations in lattice QCD are not applicable to $\mu/T \gg 1$ due to the sign problem, we adopt the (2+1)-flavor Nambu–Jona-Lasinio (NJL) model which captures the essential properties of QCD such as the dynamical breaking of chiral symmetry and its restoration at finite T and μ [41, 42]. The model Lagrangian we consider reads

$$\begin{aligned}
\mathcal{L}_{\mathrm{NJL}} = {} & \bar{q}(i\partial\!\!\!/ - m)q + \frac{1}{2}G_S \sum_{a=0}^{8}[(\bar{q}\lambda^a q)^2 + (\bar{q}i\gamma_5\lambda^a q)^2] \\
& - G_D[\det \bar{q}(1+\gamma_5)q + \mathrm{h.c.}] - \frac{1}{2}g_V(\bar{q}\gamma^\mu q)^2 \\
& + \frac{H}{2}\sum_{I,A=2,5,7}(\bar{q}i\gamma_5\lambda^I\tau^A C\bar{q}^T)(q^T Ci\gamma_5\lambda^I\tau^A q) \\
& + \frac{G'_D}{8}\sum_{i,j,k=1,2,3}[(q\tilde{\lambda}_i\tilde{\tau}_k(1+\gamma_5)C\bar{q}^T) \\
& (\bar{q}\tilde{\lambda}_j\tilde{\tau}_k(1+\gamma_5)Cq)(\bar{q}_i(1+\gamma_5)q_j) + \mathrm{h.c.}],
\end{aligned}$$

where the quark field q_i^α has three colors labeled by α and three flavors labeled by i with the current quark masses m_i. The term proportional to G_S is a $U(3)_L \times U(3)_R$ symmetric four-fermi interaction where λ^a are the Gell-Mann matrices in flavor space with $\lambda^0 = \sqrt{2/3}$ I. The term proportional to G_D is called as the Kobayashi-Maskawa-'t Hooft (KMT) coupling which breaks $U(1)_A$ symmetry explicitly [43, 44]. The term proportional to $g_V (\geq 0)$ gives a universal repulsive force among different flavors. The term proportional to H gives a diquark condensation with color anti-triplet, flavor anti-triplet and $J^P = 0^+$ channel where $C = i\gamma_2\gamma_0$ is the charge conjugation matrix and τ^a are the Gell-Mann matrices in color space with $\tau^0 = \sqrt{2/3}$ I. The term proportional to G'_D is obtained by the Fierz transformation of the KMT term and gives a coupling between the chiral condensate and the diquark condensate. Here we have introduced a notation, $\tilde{\lambda}_{1,2,3} \equiv \lambda_{7,5,2}$ and $\tilde{\tau}_{1,2,3} \equiv \tau_{7,5,2}$.

In the mean-field approximation, the constituent quark masses M_i and the gap parameters Δ_i are generated dynamically through the NJL interactions,

$$M_i = m_i - 2G_S\sigma_i + 2G_D\sigma_j\sigma_k + \frac{G'_D}{4}|s_i|^2, \tag{1}$$

$$\Delta_i = -\left(H - \frac{G'_D}{2}\sigma_i\right)s_i, \tag{2}$$

where $\sigma_i = \langle\bar{q}_i q_i\rangle$ is the chiral condensate in each flavor, $s_i = \langle\bar{q}^T C\gamma_5\tilde{\lambda}_i\tilde{\tau}_i q\rangle$ is the diquark condensate in each color and flavor with (i, j, k) corresponding to the cyclic permutation of u, d and s. The thermodynamic potential Ω is related to the pressure as $\Omega = -T\log Z = -PV$ with P given by

$$\begin{aligned}
P(T, \mu_{u,d,s}) = {} & \frac{T}{2}\sum_\ell \int \frac{d^3p}{(2\pi)^3}\mathrm{Trln}\left(\frac{S^{-1}(i\nu_\ell, \mathbf{p})}{T}\right) \\
& - G_S\sum_i \sigma_i^2 - 4G_D\sigma_u\sigma_d\sigma_s + \frac{g_V}{2}\left(\sum_i n_i\right)^2 \\
& - \sum_{i=1,2,3}\frac{1}{2}(H - G'_D)|s_i|^2.
\end{aligned}\tag{3}$$

Here $i\nu_\ell = (2\ell+1)\pi T$ is the Matsubara frequency, $n_i = \langle q_i^\dagger q_i\rangle$ is the quark number density in each flavor, and S is the quark propagator in the Nambu-Gor'kov representation,

$$\left[S^{-1}\right]^{ij}_{\alpha\beta} = \begin{pmatrix} [G_0^+]^{-1} & \sum_{i=1,2,3}\Delta_i\gamma_5\tilde{\lambda}_i\tilde{\tau}_i \\ -\sum_{i=1,2,3}\Delta_i^*\gamma_5\tilde{\lambda}_i\tilde{\tau}_i & [G_0^-]^{-1} \end{pmatrix},$$

where

$$[G_0^\pm]^{-1} = p\!\!\!/ - \hat{M} \pm \gamma_0\hat{\mu}^{\mathrm{eff}}. \tag{4}$$

Here, $\hat{M}$ is a unit matrix in color space and a diagonal matrix in flavor space, diag(M_u, M_d, M_s). The effective chemical potential matrix $\hat{\mu}^{\mathrm{eff}}$ is defined from

$$\hat{\mu}^{\mathrm{eff}} \equiv \hat{\mu} - g_V\sum_j n_j, \tag{5}$$

where each component of $\hat{\mu}$ is given by

$$\mu^{ij}_{\alpha\beta} = (\mu\delta^{ij} + \mu_Q Q^{ij})\delta_{\alpha\beta} + (\mu_3(\tau_3)_{\alpha\beta} + \mu_8(\tau_8)_{\alpha\beta})\delta^{ij}.$$

There are nine independent parameters in the (2+1)-flavor NJL model; the UV cutoff, Λ, the coupling constants, G_S, G_D, g_V, H and G'_D and the current quark masses, $m_{u,d}$ and m_s. Five parameters except for g_V, H and G'_D have been determined from hadron phenomenology in the vacuum. In this article, we adopt the HK parameter set [41] (results for other parameter sets, see [16]):

$$\begin{aligned}
& \Lambda = 631.4\,\mathrm{MeV},\ G_S\Lambda^2 = 3.67,\ G_D\Lambda^5 = 9.29, \\
& m_{u,d} = 5.5\,\mathrm{MeV},\ m_s = 135.7\,\mathrm{MeV}.
\end{aligned}\tag{6}$$

For g_V, we change its magnitude in the following range [45, 46]:

$$0 \leq \frac{g_V}{G_S} \leq 0.5. \tag{7}$$

The parameters H and G'_D are chosen to be $H = G_S$ and $G'_D = G_D$ as characteristic values. (Corresponding values from the Fierz transformation are $H = \frac{3}{4}G_S$ and $G'_D = G_D$. For extensive analyses with other choice of parameters in the diquark channels, see [47–49].)

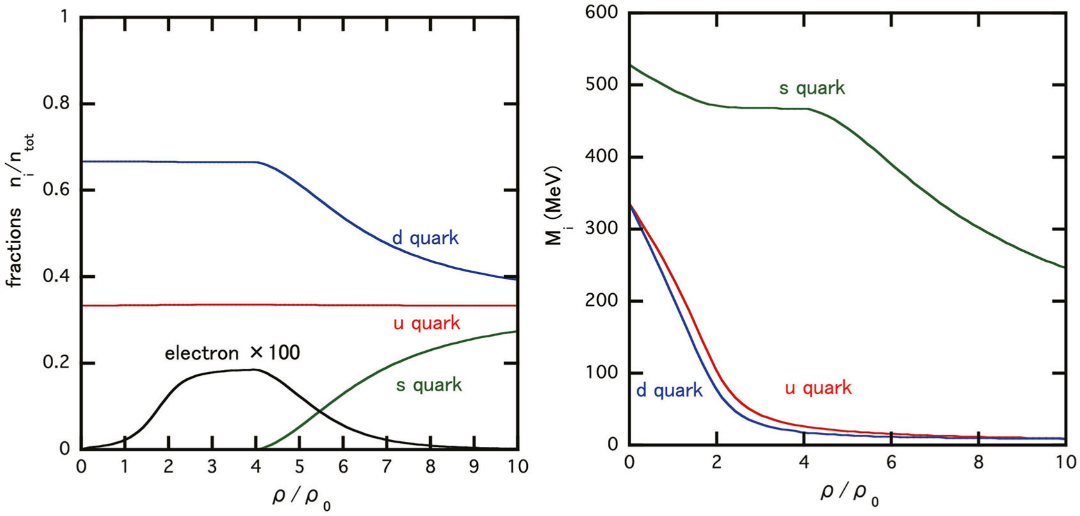

(a) (b)

Fig. 3. (a) The number fractions ($n_{u,d,s,e}/n_{\rm tot}$ with $n_{\rm tot} = n_u + n_d + n_s = 3\rho$) as a function of the baryon density ρ. Red, blue and green lines correspond to u, d and s quark, respectively. The black line corresponds to the electron number fraction × 100. Muon does not appear due to the emergence of s quarks. (b) The constituent quark masses (M_i) as a function of ρ. Colors on each line are the same with those in (a). These figures are adapted from [16].

The EOS of quark matter with strangeness is obtained from the above model under three conditions: i) the charge neutrality among quarks and leptons, $\frac{2}{3}n_u - \frac{1}{3}n_d - \frac{1}{3}n_s - n_e - n_\mu = 0$, ii) the color neutrality among quarks, $n_r = n_g = n_b$, and iii) the β-equilibrium among quarks and leptons, $\mu_d = \mu_s = \mu_u + \mu_e$ and $\mu_e = \mu_\mu$. The ground state of the system is obtained by searching the maximum of the pressure in eq. (3), with the conditions

$$\frac{\partial P}{\partial \sigma_{u,d,s}} = \frac{\partial P}{\partial \Delta_{1,2,3}} = \frac{\partial P}{\partial \mu_{3,8}} = 0. \tag{8}$$

Let us first discuss a composition of the β-equilibrated quark matter at $T = 0$ without color superconductivity ($H = G'_{_D} = 0$). In fig. 3(a), the number fractions ($n_{u,d,s,e}/n_{\rm tot}$ with $n_{\rm tot} = n_u + n_d + n_s = 3\rho$) as a function of the baryon density ρ are plotted. In fig. 3(b), the constituent quark masses (M_i) as a function of ρ are plotted. These figures do not depend on the magnitude of the vector-type interaction $g_{_V}$ because the flavor-independent $g_{_V}$-type interaction leads to a pressure in eq. (3) depending only on $\mu^{\rm eff}_{\alpha,a}$.

At low densities, the s quark appears only above $\rho_{\rm th} \simeq 4\rho_0$ due to its heaviness as can be seen from fig. 3(a): Here $\rho_{\rm th}$ is determined by the condition, $\mu_s(\rho_{\rm th}) = M_s(\rho_{\rm th})$. The dynamical masses of u and d quarks decrease rapidly below $\rho_{\rm th}$ due to partial restoration of chiral symmetry, while the s quark is affected only a little through the KMT interaction as seen from fig. 3(b). Once the s-quark whose electric charge is negative starts to appear above $\rho_{\rm th}$, the number of electrons decreases to satisfy the charge neutrality. Since the electron chemical potential does not exceed the muon mass 106 MeV, the muons do not appear even at high density. In the high density limit, the system approaches to the flavor symmetric u, d, s matter without leptons.

Once the interactions in the diquark channels (H and $G'_{_D}$) are switched on, the color superconductivity (CSC) develops as shown in fig. 4(a), where the gap parameters Δ_i as a function of the quark chemical potential μ with $g_{_V}/G_{_S} = 0.5$ are plotted. The red line corresponds to the ud pairing, and blue line corresponds to the ds or su pairings. With $H/G_{_S} = 1$, two-color superconductivity (2SC) appears as soon as the baryon density of the quark matter becomes finite at $\mu = 335$ MeV. Then the first-order transition from the 2SC to the color-flavor-locking (CFL) phase takes place at around $\mu = 520$ MeV. The diquark condensates affect the behavior of the number fractions ($n_{i,e}/n_{\rm tot}$) and the constituent quark masses (M_i) through the coupled equations, eq. (8): Those are taken into account into the following calculations with CSC.

Figure 4(b) shows the thermodynamic quantities (P and ε) as a function of ρ in the (2+1)-flavor NJL model. The red (blue) lines correspond to the case with (without) CSC. In terms of the baryon density, 2SC (CFL) appears for $2\rho_0 < \rho < 5\rho_0$ ($\rho > 5\rho_0$) in the present parameter set. The plateau of the red line (P with CSC) reflects the fact that there is a first-order transition from 2SC to CFL. As we will see later, baryon density relevant to neutron stars with the hadron-quark crossover is below $5\rho_0$. Therefore, the CFL phase barely appears in the central core of the NSs in the present model.

5 CRover: New EOS with hadron-quark crossover

We now introduce the following phenomenological interpolation of the energy per baryon $\hat{E} \equiv E/N_{_B}$ at $T = 0$ [15, 16]:

$$\hat{E}(\rho) = \hat{E}_{\rm H}(\rho) w_-(\rho) + \hat{E}_{\rm Q}(\rho) w_+(\rho), \tag{9}$$

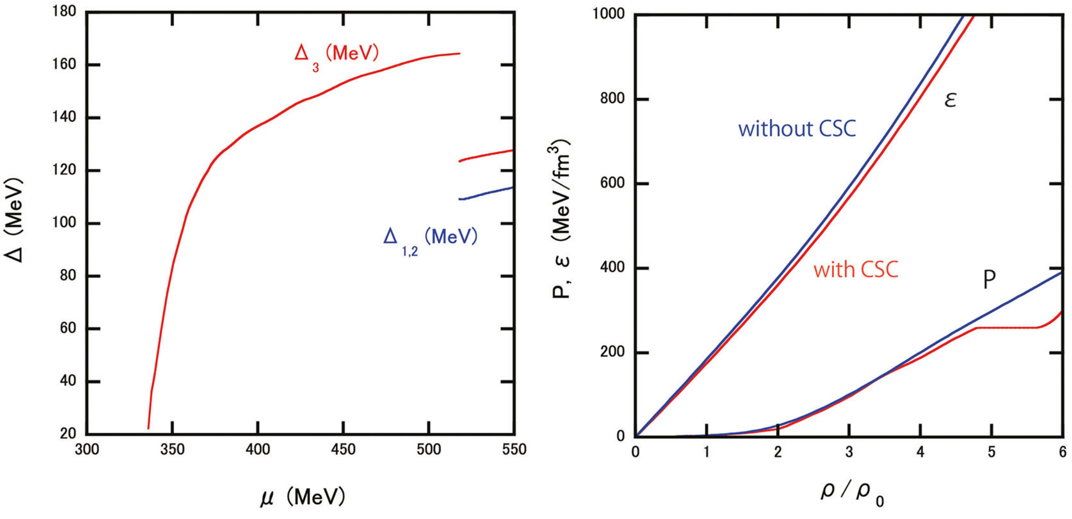

(a) (b)

Fig. 4. (a) The gap parameters Δ_i $(i = 1, 2, 3)$ as a function of the quark chemical potential μ. Solid red line: Δ_3 corresponding to the pairing between u quark and d quark. Solid blue line: Δ_1 and Δ_2 corresponding to the ds pairing and su pairing, respectively. (b) The energy density (ε) and pressure (P) as a function of baryon number density ρ. The red lines show the quark EOSs with diquark condensate. The blue lines show the quark EOSs without diquark condensate.

where $\hat{E}_{\rm H}$ and $\hat{E}_{\rm Q}$ represent energy per baryon in the hadronic matter with leptons and that in the quark matter with leptons, respectively. w_- and $w_+ = 1 - w_-$ are the weight functions

$$w_\pm(\rho) \equiv \frac{1}{2}\left(1 \pm \tanh\left(\frac{\rho - \bar{\rho}}{\Gamma}\right)\right), \tag{10}$$

where $\bar{\rho}$ and Γ are the phenomenological parameters which characterize the averaged crossover density and the width of the crossover window, respectively. Similar weight function has been previously used to interpolate the hadronic phase and the quark-gluon plasma at finite temperature [50,51]. The window $\bar{\rho} - \Gamma \lesssim \rho \lesssim \bar{\rho} + \Gamma$ characterizes the crossover region in which both hadrons and quarks are strongly interacting, so that neither pure hadronic EOS nor pure quark EOS are reliable.

The other observables can be obtained by using the thermodynamic relations from $\hat{E}(\rho) = \varepsilon/\rho$,

$$P = \rho^2 \frac{\partial \hat{E}}{\partial \rho}, \quad \mu = \frac{\partial \varepsilon}{\partial \rho}, \quad K = \rho \frac{\partial P}{\partial \rho},$$
$$v_s^2(\rho) = \frac{\partial P}{\partial \varepsilon} = \frac{K}{\varepsilon + P}. \tag{11}$$

Here K is the bulk modulus which must be positive semi-definite for thermodynamic stability. Also, v_s is the sound velocity which is a characteristic measure of the stiffness of the EOS.

In fig. 5(a), we show the interpolated EOS at $T = 0$ (cold CRover EOS) with the TNI2u as a hadronic EOS and the NJL with $g_V = 0$ $(g_V = 0.5G_S)$ as a quark EOS. The diquark condensates are switched off here $(H = G'_D = 0)$. The sound velocity squared as a function of ρ is shown in fig. 5(b). In both figures, the onset of the strangeness is indicated by the filled circles. From both figures, one finds that the CRover EOS becomes stiffer than the quark phase and the hadronic phase in the crossover region indicated by the shaded band. Such stiffening is induced by the extra pressure originating from the derivative of ρ acting on $w_\pm(\rho)$ in eq. (11):

$$P(\rho) = P_{\rm H}(\rho)w_-(\rho) + P_{\rm Q}(\rho)w_+(\rho) + \Delta P(\rho). \tag{12}$$

The extra pressure ΔP is required from thermodynamic consistency and has a property, $\Delta P(\rho = 0) = \Delta P(\rho = \infty) = 0$ by definition, *i.e.* it is a function localized in the crossover region.

By turning on CSC with $H = G_S$ and $G'_D = G_D$, the interpolated EOS becomes a little bit softer than the case without CSC in the crossover region as shown by the red lines in fig. 6(a) and (b). Associated with this, the onset density of the strangeness is reduced from 4ρ to $3.6\rho_0$. As we have discussed in sect. 4, there is little room for the CFL phase to appear inside NSs in our CRover EOS, it is not considered in this figure.

6 Neutron Stars with CRover EOS at $T = 0$

We study the structure of the spherically symmetric neutron stars in hydrostatic equilibrium by solving the Tolman-Oppenheimer-Volkov (TOV) equation;

$$\frac{dP}{dr} = -\frac{G}{r^2}\left(M(r) + 4\pi P r^3\right)(\varepsilon + P)\left(1 - 2GM(r)/r\right)^{-1},$$
$$M(r) = \int_0^r 4\pi r'^2 \varepsilon(r') dr'. \tag{13}$$

Here r being the radial distance from the center and G is the gravitational constant.

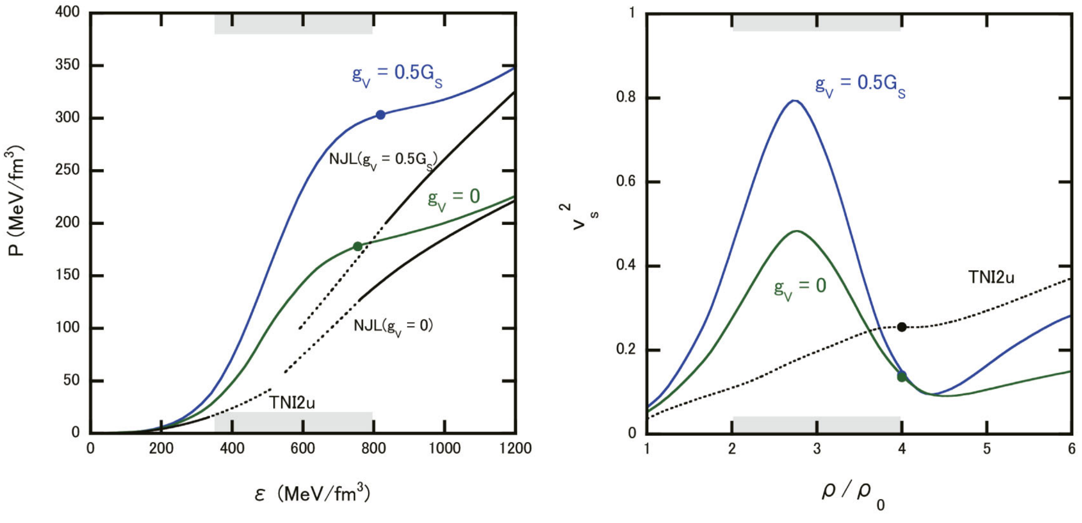

(a) (b)

Fig. 5. (a) The relation between the interpolated energy density and the resultant pressure for $g_V = 0$ (green) and $g_V = 0.5G_S$ (blue) without CSC, $H = G'_D = 0$. The crossover window is (2–4)ρ_0. The filled circle denotes the threshold density of the strangeness. (b) Sound velocity squared v_s^2 as a function of baryon density ρ. Solid lines show $v_s - \rho$ obtained from the interpolated EOS with $g_V/G_S = 0, 0.5$, while the dotted line corresponds to the TNI2u hadronic EOS. The filled circles denote the points beyond which strangeness starts to appear. Those figures are adapted and modified from [16].

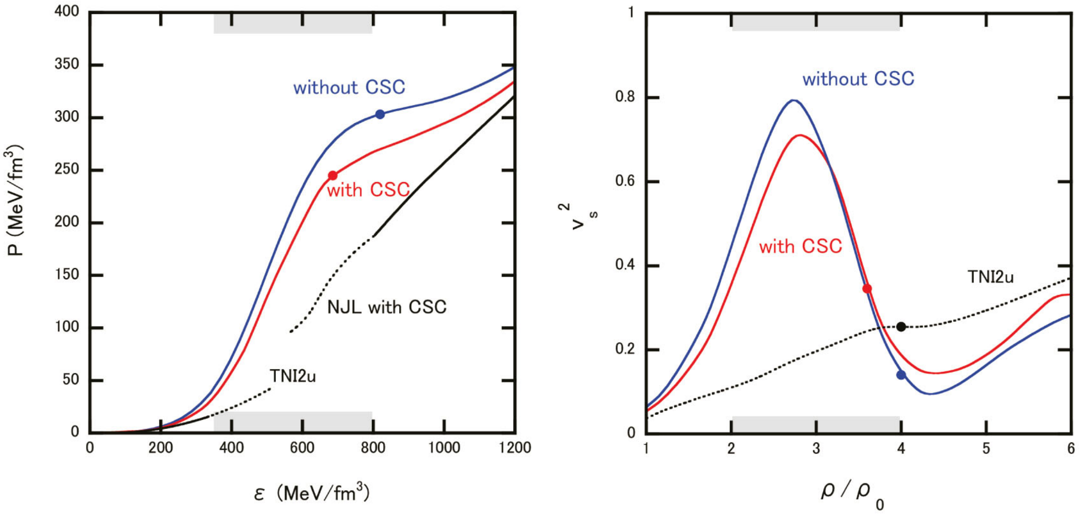

(a) (b)

Fig. 6. (a,b) Comparison between the CRover EOS and the sound velocity squared without CSC ($H = G'_D = 0$) and those with CSC ($H = G_S$ and $G'_D = G_D$) for $g_V/G_S = 0.5$.

6.1 Case without color superconductivity

First, we consider the case without the diquark condensate ($H = G'_D = 0$) as a baseline. In fig. 7(a), we plot the M-ρ_c relation from the CRover EOS (interpolation between the TNI2u hadronic EOS and the NJL quark EOS with $g_V/G_S = 0, 0.5$ in the crossover region $(\bar{\rho}, \Gamma) = (3\rho_0, \rho_0)$). For comparison, the M-ρ_c relation only with TNI2u hadronic EOS is plotted by the dotted line. Figure 7(b) shows the corresponding M-R relation for the same EOSs as fig. 7(a). Strong correlation between the sudden stiffness of the sound velocity in fig. 5(b) and the NS masses in fig. 7(a,b) can be seen. Also, as g_V increases from zero, the quark EOS and hence the CRover EOS become stiffer, which increases the maximum mass (indicated by the cross symbol) beyond $2M_\odot$. We emphasize that these qualitative features do not depend on the details of the interpolation method. Smooth and thermodynamically consistent interpolations between the "soft" EOS at low density and relatively "stiff" EOS at high density always lead to the sudden stiffening in the crossover region as characterized by the sound velocity in fig. 5(b).

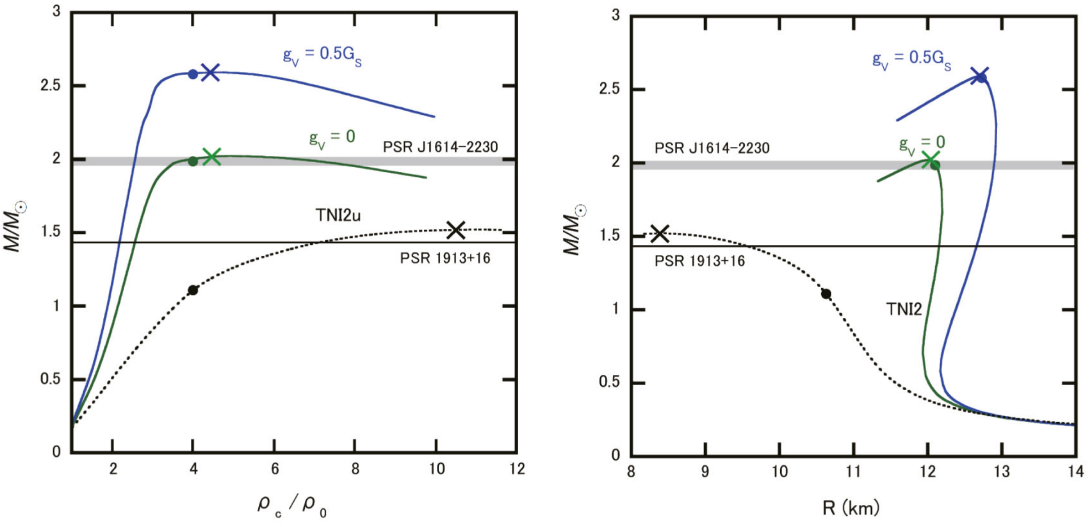

(a) (b)

Fig. 7. (a) The M-ρ_c relations with the CRover EOS (solid lines) and the TNI2u hadronic EOS (the dotted line). The crossover window is fixed to be $(\bar{\rho}, \Gamma) = (3\rho_0, \rho_0)$. The cross symbols denote the points of $M_{\max}$, while the filled circles denote the points beyond which the strangeness appears. The gray band denotes $M = (1.97 \pm 0.04)M_\odot$ for PSR J1614-2230. The solid black line denotes $M = 1.44M_\odot$ for PSR 1913+16. (b) The M-R relations with the same EOSs as (a). These figures are adapted from [16].

This is in sharp contrast to the case of the first-order phase transition where the EOS always becomes soft in the mixed phase.

One important aspect of the present result is that the radii of NSs are confined in a narrow range: For example, in the case of $g_V/G_S = 0(0.5)$, all the NSs with $0.5 < M/M_\odot < 2.0$ ($0.5 < M/M_\odot < 2.5$) have the radius in the range $R = (12.0 \pm 0.2)\,\mathrm{km}$ ($R = (12.5 \pm 0.5)\,\mathrm{km}$). This universal feature of the radius is primarily caused by the interpolation to the Q-EOS as seen by comparing the dashed line and the solid lines in fig. 7(b). Also, the radius tends to become larger as the Q-EOS becomes stiffer. The narrow window of R almost independent of the values of M will confront the present and future observations of the neutron star radii [52,53].

Another important aspects of the present result is the onset of the strangeness inside the NS core as indicated by the filled circles in fig. 7(b): The strangeness appears only in very massive NSs with nearly the maximum mass if we have hadron-quark crossover. In fact, $\rho_c = 2.4\rho_0$ for $2M_\odot$ while $\rho_c = 4.4\rho_0$ for $2.59M_\odot$ under the CRover EOS with $g_V = 0.5G_S$, so that even the observed $2M_\odot$ NSs are unlikely to have strangeness inside.

6.2 Case with color superconductivity

In fig. 8(a,b), M-ρ_c and M-R relations are plotted by using the CRover EOS with and without CSC given in fig. 6(a). For comparison, the results of the TNI2u hadronic EOS are shown by the black dotted lines. As we discussed in the last section, the CSC softens the EOS. Then, the $M_{\max}$ of the NS with CSC becomes smaller by $0.2M_\odot$ than that without CSC phase. Such a reduction of $M_{\max}$ due to CSC is consistent with other calculations (see, *e.g.*, [54,55]).

Two remarks are in order here about the effect of CSC on the M-R relations: i) The central density of the NSs does not exceed $4.9\rho_0$ in CRover EOS with CSC, so that the CFL phase barely appears inside the star. ii) The effect of 2SC already becomes visible for low-mass stars ($M < 0.5M_\odot$) with the central density below $2\rho_0$. This is because we have a smooth interpolation between the hadronic EOS and quark EOS, so that the 2SC component has small but non-negligible contribution even below $2\rho_0$. Physically, this could be interpreted as partial percolation of the nucleons into quarks with strong diquark correlations.

Table 2 is a summary of the maximum mass $M_{\max}$ and the central density ρ_c normalized by ρ_0 with the CRover EOS. Two sets of hadronic EOS (TNI2u and TNI2) are adopted, but the difference is small. The strength of the repulsive vector interaction g_V and the crossover density $\bar{\rho}$ are changed to see the sensitivity of the results. As g_V becomes larger and the $\bar{\rho}$ becomes smaller, the maximum mass $M_{\max}$ increases due to the presence of the quark matter. The effect of CSC generally decreases $M_{\max}$ and increases ρ_c. As long as $\bar{\rho}$ is around $3\rho_0$, the CRover EOS can easily accommodate the $2M_\odot$ NSs.

7 Neutron star with CRover EOS at T $\neq$ 0

In this section, we describe the properties of hot neutron stars created after the core-collapsed Type-II supernova explosion by generalizing the idea of the hadron-quark crossover discussed in the previous sections (for details, see [17]).

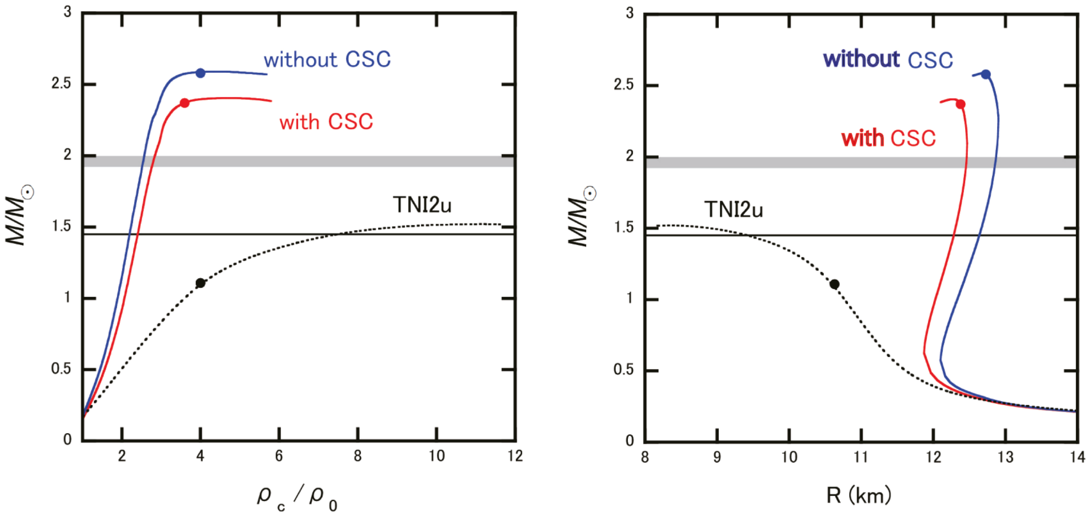

(a) (b)

Fig. 8. (a) The M-ρ_c relations with the CRover EOS (solid lines) and TNI2u hadronic EOS (dotted line) with and without the CSC phase for $g_V/G_S = 0.5$. (b) The M-R relations with the same EOSs as (a).

Table 2. $M_{\max}/M_\odot$ (ρ_c/ρ_0) for different choices of hadronic EOS, quark EOS and the crossover window.

	$g_V = 0$ without CSC		$g_V = 0.5G_S$ without CSC		$g_V = 0.5G_S$ with CSC
$(\bar{\rho}, \Gamma)$	$(3\rho_0, \rho_0)$	$(5\rho_0, 2\rho_0)$	$(3\rho_0, \rho_0)$	$(5\rho_0, 2\rho_0)$	$(3\rho_0, \rho_0)$
TNI2u	2.02 (4.5)	1.86 (8.7)	2.59 (4.4)	2.25 (6.1)	2.40 (4.9)
TNI2	2.02 (5.8)	1.84 (9.1)	2.59 (4.3)	2.23 (6.8)	2.40 (4.8)

During the first few seconds after the core bounce, the proto-neutron star with the radius $\sim 200\,\text{km}$ is formed. It undergoes a rapid contraction and evolves into a "hot" neutron star with the radius $\sim 20\,\text{km}$ in about 1 second (or to a black hole). The hot NS at birth in quasi-hydrostatic equilibrium is characterized by the supernova matter with the lepton fraction, $Y_l = Y_e + Y_\nu \sim 0.3$–$0.4$, and the entropy per baryon, $S/N = \hat{S} \sim 1$–2. The neutrinos are trapped inside the hot NSs and contribute to the β-equilibrium. With this as an initial condition, the hot NS contracts gradually by the neutrino diffusion with the time scale of 10-100 seconds and evolves to a nearly "cold" NS with $Y_\nu \simeq 0$ and $\hat{S} \simeq 0$, unless another collapse to a black hole does not take place [56–58].

Thermal properties of the hot NSs are intimately related to the physics of high density matter at finite temperature. Indeed, the hot NSs with the hadron-quark mixed phase (fig. 1(a)) have been studied previously, *e.g.* [59–62]. It is then interesting to explore properties of the hot NSs (such as the M-R relation and the profiles of the temperature, density and sound velocity inside the star etc.) with hadron-quark crossover (fig. 1(b)).

In fig. 9, we show a schematic picture which compares the internal structure of the hot and cold NSs with $2M_\odot$. Above the normal nuclear matter density ρ_0, we use the EOS interpolated between TNI2 (hadron) and NJL (quark). On the other hand, below ρ_0, we use the thermal EOS which consists of an ensemble of nuclei and interacting nucleons in nuclear statistical equilibrium given by Hempel and Schaffner-Bielich (HS EOS) [63]. (Use of other EOSs below ρ_0 does not show quantitative difference as discussed in [64].) Once the baryon density becomes smaller than the neutron drip density $10^{-3}\rho_0$, the temperature becomes smaller than 0.1 MeV. Then we switch to the standard BPS EOS [65].

7.1 Supernova matter at finite T

Major differences of the supernova matter from that of the cold matter discussed in previous sections are i) the diffused Fermi surface due to the effect of T, ii) the existence of degenerate neutrinos, and iii) the contributions from anti-particles.

By neglecting the strangeness in hadronic matter and the muon which are irrelevant for stiff EOS, we consider a system composed of n, p, e^-, e^+, ν_e and $\bar{\nu}_e$ in the hadronic EOS at finite T, and u, d, s, e^-, e^+, ν_e and $\bar{\nu}_e$ in the quark EOS at finite T. The charge neutrality, chemical equilibrium and baryon and lepton number conservations are imposed. In practice, we find $\mu_e/T > 15$ in the interior of the hot NSs, so that the effects of e^+ and $\bar{\nu}_e$ (as well

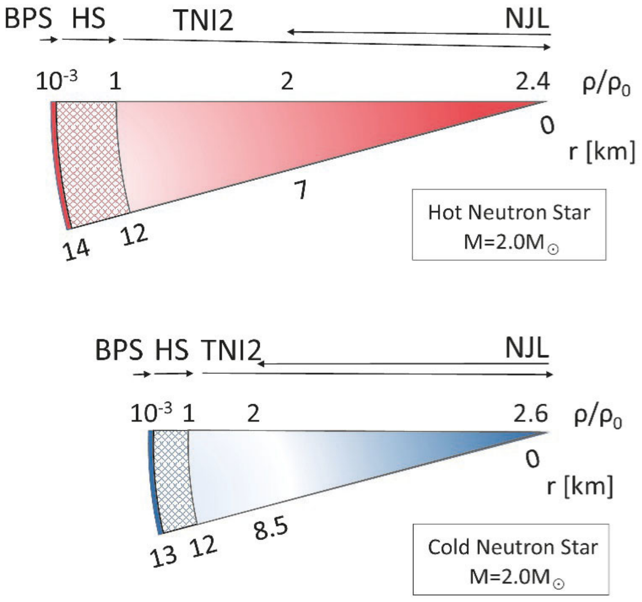

Fig. 9. Comparison between the hot NS and cold NS with $M = 2M_\odot$ obtained by the CRover EOS with $g_V = 0.5G_S$. We take $(Y_l, \hat{S}) = (0.3, 1)$ to characterize the hot NS. As for the details of the EOSs adopted at different densities, BPS, HS, TNI2 and NJL, see the text. This figure is adapted from [17].

as neutrinos in second and third generations) are negligibly small. The color superconductivity is switched off for simplicity.

We use the Helmholtz free-energy per baryon $\hat{F} = F/N_B = \hat{E} - T\hat{S}$ as a basic quantity to interpolate the hadronic matter and the quark matter at finite T [17]. This is a natural generalization of $\hat{E}$ at $T = 0$ in the previous sections. $\hat{F}$ is a function of ρ, T and Y_l, so that we have

$$\hat{F}(\rho, T; Y_l) = \hat{F}_{\rm H}(\rho, T; Y_l) w_-(\rho, T) + \hat{F}_{\rm Q}(\rho, T; Y_l) w_+(\rho, T). \qquad (14)$$

Here $\hat{F}_{\rm H}$ and $\hat{F}_{\rm Q}$ are the hadron+lepton free-energy per baryon and the quark+lepton free-energy per baryon, respectively. The typical temperature of hot NSs is about 30 MeV which is sufficiently smaller than the thermal dissociation temperature of hadrons of about 200 MeV. Therefore, we ignore the T dependence of the weight functions, $w_\pm(\rho, T) \to w_\pm(\rho)$.

The entropy per baryon and the energy per baryon are obtained by using the thermodynamic relations, $\hat{S} = -\partial\hat{F}/\partial T$ and $\hat{E} = \hat{F} + T\hat{S}$. Under the assumption that $w_\pm$ is T-independent, eq. (14) leads to

$$\hat{S}(\rho, T; Y_l) = \hat{S}_{\rm H}(\rho, T; Y_l) w_-(\rho) + \hat{S}_{\rm Q}(\rho, T; Y_l) w_+(\rho),$$
$$\hat{E}(\rho, T; Y_l) = \hat{E}_{\rm H}(\rho, T; Y_l) w_-(\rho) + \hat{E}_{\rm Q}(\rho, T; Y_l) w_+(\rho).$$

To obtain $\hat{F}_{\rm H}$ in eq. (14), we solve the thermal Hartree-Fock equation for isothermal matter composed of n, p, e^-, e^+, ν_e and $\bar{\nu}_e$ with the same effective nucleon interaction as the TNI2 and TNI2u EOS at $T = 0$ (details are shown in [66]). To obtain $\hat{F}_{\rm Q}$ in eq. (14), we start with the Gibbs free energy calculated in the NJL model in sect. 4; $\Omega_{\rm Q}(\mu, V, T; \mu_l) = \Omega_{\rm quark}(\mu, V, T; \mu_l) + \Omega_{\rm lepton}(\mu, V, T; \mu_l)$ with μ and μ_l being the baryon chemical potential and the lepton chemical potential, respectively. Then we make the Legendre transformation from the Gibbs free energy $\Omega_{\rm Q}$ to the Helmholtz free-energy $F_{\rm Q}$ [17].

In the following, we consider typical values of the lepton fraction $Y_l = 0.3, 0, 4$ and those of the entropy per baryon $\hat{S} = 1, 2$. The crossover window is fixed to be $(\bar{\rho}, \Gamma) = (3\rho_0, \rho_0)$, and $g_V = 0.5G_s$ is adopted.

The thermodynamic quantities for isothermal matter with ρ, T and Y_l as parameters can be converted into those for isentropic matter with ρ, S and Y_l as parameters by using the relation $T = T(\rho; S, Y_l)$. In fig. 10(a), the temperature T of the isentropic matter is shown as a function of the baryon density ρ for $Y_l = 0.3$ with $\hat{S} = 1$ and $\hat{S} = 2$.

The isentropic pressure is obtained through the thermodynamic relation

$$P(\rho, T(\rho; S, Y_l); Y_l, \hat{S}) = \rho^2 \left.\frac{\partial \hat{E}}{\partial \rho}\right|_{\hat{S}, N, Y_l}. \qquad (15)$$

The hot CRover EOS for supernova matter is shown in fig. 10(b) for $(Y_l, \hat{S}) = (0.3, 1), (0.3, 2)$ and $(0.4, 1)$. For comparison, the cold CRover EOS for cold neutron star matter ($T = 0$ without neutrino degeneracy) is shown by the black solid lines. The hot CRover EOS and cold CRover EOS are similar except for the low density region where the hot EOS becomes stiffer.

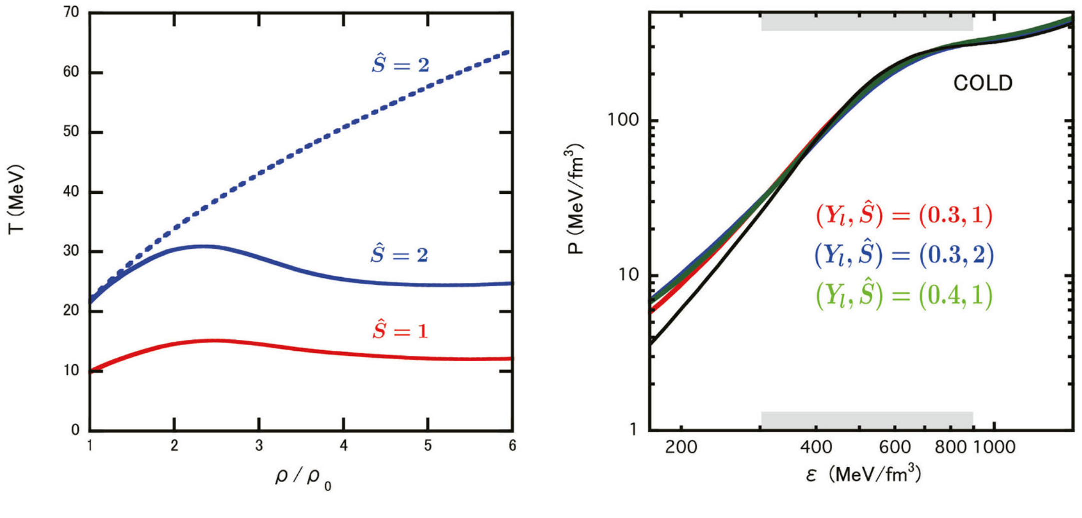

(a) (b)

Fig. 10. (a) The temperature T of the isentropic matter as a function of the baryon density ρ for $Y_l = 0.3$ with $\hat{S} = 1$ (red) and $\hat{S} = 2$ (blue) in hot CRover EOS. The dashed line corresponds to the hot TNI2 EOS only with hadrons and leptons. (b) The isentropic pressure P of hot CRover EOS as a function of ε for $(Y_l, \hat{S}) = (0.3,\ 1)$, $(0.3,\ 2)$ and $(0.4,\ 1)$. The black line corresponds to the cold CRover EOS for cold neutron star matter. The crossover window is shown by the shaded area on the horizontal axis. These figures are adapted from [17].

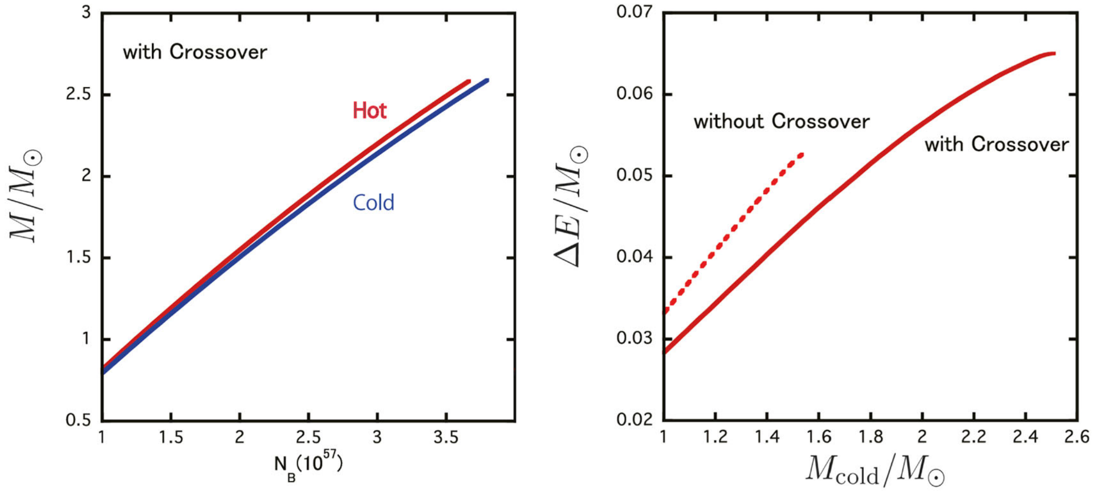

(a) (b)

Fig. 11. (a) The neutron star mass M as a function of the total baryon number N_B in CRover EOS. Red and blue curves correspond to the hot and cold neutron stars, respectively. (b) The energy release (estimated under the conservation of N_B) $\Delta E = M_{\rm hot} - M_{\rm cold}$ as a function of the cold neutron star mass $M_{\rm cold}$. $(Y_l, \hat{S}) = (0.3, 1)$ is adopted. These figures are adapted from [17].

7.2 Properties of hot NSs

Figure 11(a) shows the gravitational mass M as a function of the total baryon number N_B for hot (red line) and cold (blue line) neutron stars. The hot neutron stars have larger mass than the cold ones for given N_B. We note that the maximum value of N_B for hot NSs is smaller than that for cold NSs. This implies that hot NSs do not have a chance of delayed collapse into black holes after the cooling. This is in contrast to the previous works with the exotic phases such as the pion condensation [67] and the hadron-quark mixed phase [59,61]; in those cases, the softening of the EOS due to exotic phases is tamed by the finite temperature effect, so that the maximum value of N_B for hot NS becomes larger than that of the cold NS and there arises a chance of the delayed collapse.

In fig. 11(b), we show $\Delta E = M_{\rm hot} - M_{\rm cold}$ in the unit of $M_\odot$ as a function of the mass of cold NS, $M_{\rm cold}$. The typical amount of energy released due to the contraction is about $0.04M_\odot \simeq 7.2 \times 10^{52}$erg for $M_{\rm cold} = 1.4M_\odot$. This energy release from the hot NSs to cold NSs with crossover is about 25% smaller than that without the crossover [67].

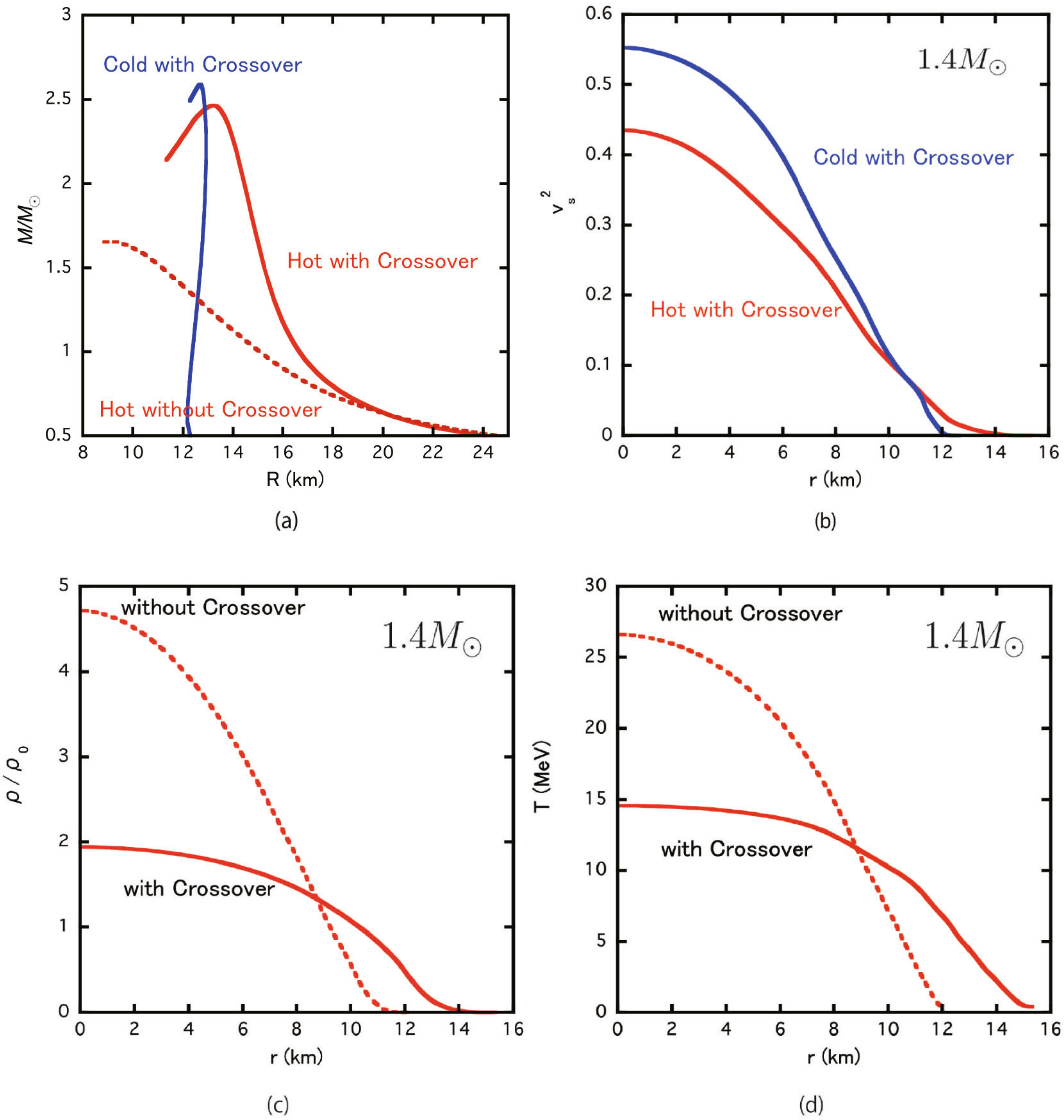

Fig. 12. (a) Mass-radius (M-R) relationship for $(Y_l, \hat{S}) = (0.3, 1)$. Red solid line: hot neutron stars with hot CRover EOS. Blue solid line: cold neutron stars with cold CRover EOS. Red dashed line: hot neutron stars without crossover. (b) The sound velocity squared v_s^2 as a function of the distance from the center r of $1.4M_\odot$ neutron star. Colors on each line are the same as in (a). (c) The density profiles of the hot neutron star with $M = 1.4M_\odot$ and $(Y_l, \hat{S}) = (0.3, 1)$. Solid and dashed lines correspond to the EOS with crossover and without crossover, respectively. (d) The temperature profiles of the same neutron star as plotted in (c). These figures are adapted from [17].

In fig. 12(a), we plot the M-R relations for hot and cold NSs with and without crossover. The maximum mass of hot NSs is very similar with that of cold NSs. On the other hand, a big difference of the radius can be seen between hot and cold NSs. This comes from the stiffening of the hot EOS at densities below ρ_0. The maximum rotation rate given by the spin-up rate from hot NSs can gives a more stringent condition than the Keplerian angular frequency [67]. The spin-up rate of NSs with the crossover can be calculated as about 14% (assuming the conservation of angular momentum) for $M_{\mathrm{cold}} = 1.4M_\odot$ of evolved cold NSs. However, there are a small difference between NSs with and without the crossover.

The local sound velocity squared $v_s^2(r)$ for isentropic matter can be calculated as

$$v_s^2(\rho; Y_l, \hat{S}) = \left.\frac{\partial P}{\partial \varepsilon}\right|_{Y_l,\hat{S}} = \left.\frac{\mathrm{d}P(\rho, T(\rho); Y_l, \hat{S})/\mathrm{d}\rho}{\mathrm{d}\varepsilon(\rho, T(\rho); Y_l, \hat{S})/\mathrm{d}\rho}\right|_{Y_l,\hat{S}}, \qquad (16)$$

with $\rho(r)$ obtained by the TOV equation. In fig. 12(b), sound velocity squared is plotted as a function of the distance from the center r for $M = 1.4M_\odot$. The sound velocity in cold NS is larger (smaller) at higher (lower) density than that of the hot NS [17].

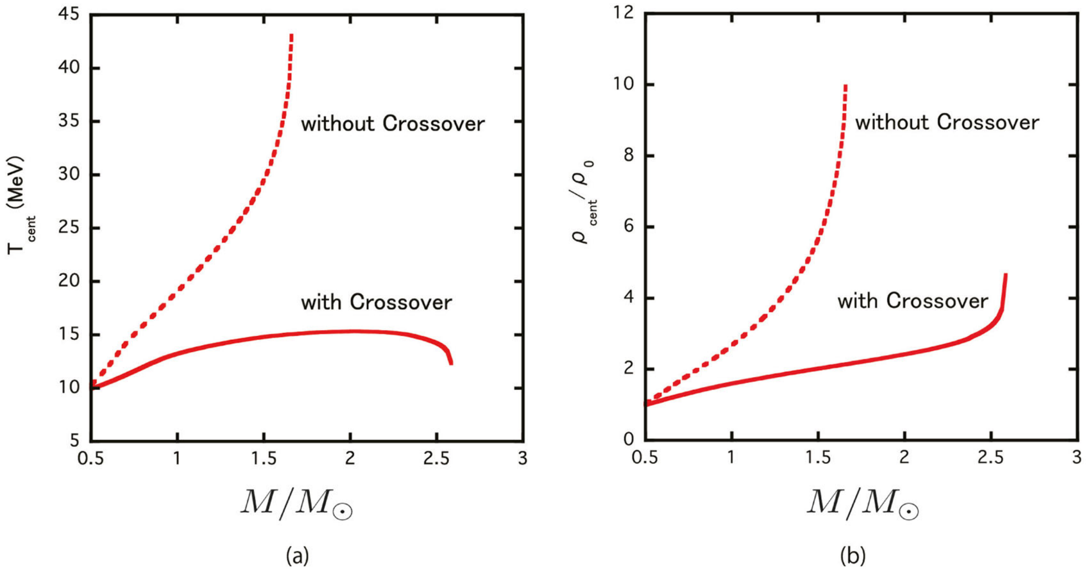

(a) (b)

Fig. 13. (a) The central temperature T_c and (b) the central density $\rho_{\rm cent}$ as a function of the neutron star mass M of hot NS with $(Y_l, \hat{S}) = (0.3, 1)$. The solid (dashed) lines correspond to the EOS with (without) crossover. These figures are adapted from [17].

To see the thermal and lepton effects on the internal structure of the hot NSs, we plot the density profile $\rho(r)$ and the temperature profile $T(r)$ of hot NSs with canonical $1.4M_\odot$ in figs. 12(c) and (d), respectively. Due to the stiffness of the CRover EOS, the central density becomes smaller and the profile becomes flatter as shown in fig. 12(c). Moreover, as we have shown in fig. 10(a), T becomes smaller for given ρ by the crossover to quark degrees of freedom. Those are the reasons why the temperature of the internal core of the hot NS becomes smaller and flatter with crossover (fig. 12(d)). This decrease of the temperature is a signal for the existence of quarks in the core of NSs.

In fig. 13(a) and (b), the central temperature $T_{\rm cent}$ and the central density $\rho_{\rm cent}$ of the hot neutron stars with and without the crossover are plotted as a function of neutron star mass M. The effects of crossover on the internal structure of the NSs shown in fig. 12(c,d) for $M = 1.4M_\odot$ can be seen for wide range of M.

8 Summary and concluding remarks

In this article, we have studied the bulk properties of cold and hot neutron stars on the basis of hadron-quark crossover picture. A new EOS, "CRover", introduced in [15–17] describes the smooth transition from hadronic matter to quark matter in a phenomenological way. The hadron-quark crossover which makes the EOS stiffer by the effect of the quark matter is in contrast to the first-order hadron-quark transition leading to the softening of the EOS.

At zero temperature, a crossover at around $3\rho_0$ leads to an EOS hard enough to sustain the $2M_\odot$ NSs. The radii of the NSs are located in a narrow region (12.5 ± 0.5) km which is insensitive to their masses. Due to the stiffening of the EOS induced by the crossover, the central density of the NSs is at most $4\rho_0$. Therefore, hyperon mixing, whose threshold density is about $4\rho_0$ in the CRover EOS, takes place only for very massive NSs. This constitutes a solution of the long-standing hyperon puzzle.

We have studied the effect of color superconductivity (CSC) on the bulk properties of NSs under the hadron-quark crossover. With the diquark coupling $H/G_S = 1$, we find that 2SC phase may appear inside the NSs while the onset of the CFL phase is too high to be realized even in massive NSs. As a result of a slight softening of the EOS due to the color superconductivity, the maximum mass of the NSs with CSC is reduced by about $0.2M_\odot$ from that without CSC.

To examine the properties of the hot NSs at birth at finite temperature, we considered the supernova matter with the CRover EOS generalized to isentropic environment. We found that the hadron-quark crossover plays an important role to lower the central temperature of hot neutron stars in comparison to the case of hadronic EOS. This suppression of temperature comes from the presence of the quark degrees of freedom in the crossover region. The radius of the hot NS with crossover is much larger that that without crossover due to the stiffness of the EOS. For example, the radius of the $1.6M_\odot$ hot NS with (without) the crossover is about 15 (10) km as shown in fig. 12(a). Such a difference could be in principle detected through the gravitational wave signal from the NS-NS binary merger, where the merging neutron stars can be reheated even up to several tens of MeV [68–70].

The hadron-quark crossover turns out to have interesting phenomenological implications to the key issues of the neutron stars, such as the massive neutron stars and hyperon puzzle, the universal radius of the neutron stars, temperature and density profiles inside the hot neutron stars, and so on. One of the most important and yet challenging theoretical problems is to elucidate the QCD basis of the phenomenological hadron-quark crossover introduced in this article.

We thank Wolfram Weise, Gordon Baym, David Blaschke and Mark Alford for helpful discussions. TT thanks Toshitaka Tatsumi, Shigeru Nishizaki and especially Ryozo Tamagaki who has passed away in Jan.11, 2015 for valuable discussions and interests in this work. KM thanks Mark Alford for the kind hospitality and discussions in Washington Univ. in St. Louis, where part of this work was carried out under the support of ALPS Program, Univ. of Tokyo. KM is also supported by JSPS Research Fellowship for Young Scientists. TH and TT were partially supported by JSPS Grant-in-Aid for Scientific Research, No.25287066. This work was partially supported by RIKEN iTHES Project.

References

1. K. Fukushima, T. Hatsuda, Rept. Prog. Phys. **74**, 014001 (2011).
2. P. Braun-Munzinger, B. Friman, J. Stachel (Editors), Nucl. Phys. A **931**, 1 (2014).
3. K. Fukushima, C. Sasaki, Prog. Part. Nucl. Phys. **72**, 99 (2013) arXiv:1301.6377 [hep-ph].
4. See, *e.g.* A. Bazavov, PoS LATTICE **2014**, 392 (2015).
5. J.M. Lattimer, Annu. Rev. Nucl. Part. Sci. **62**, 485 (2012) arXiv:1305.3510 [nucl-th].
6. P.B. Demorest, T. Pennucci, S.M. Ranson, M.S.E. Roberts, J.W.T. Hessels, Nature **467**, 1081 (2010).
7. J. Antoniadis, P.C.C. Freire, N. Wex, T.M. Tauris, R.S. Lynch, M.H. van Kerkwijk, M. Kramer, C. Bassa *et al.*, Science **340**, 6131 (2013) arXiv:1304.6875 [astro-ph.HE].
8. T. Takatsuka, T. Hatsuda, K. Masuda, in *Proceedings of the 11th International Symposium on "Origin of Matter and Evolution of Galaxies (OMEG 11)"* (Nov. 14-17, 2011, RIKEN, Wako, Japan) (2011).
9. G. Baym, Physica **96A**, 131 (1979).
10. T. Celik, F. Karsch, H. Satz, Phys. Lett. B **97**, 128 (1980).
11. T. Schafer, F. Wilczek, Phys. Rev. Lett. **82**, 3956 (1999).
12. K. Fukushima, Phys. Lett. B **591**, 277 (2004).
13. T. Hatsuda, M. Tachibana, N. Yamamoto, G. Baym, Phys. Rev. Lett. **97**, 122001 (2006) hep-ph/0605018.
14. K. Maeda, G. Baym, T. Hatsuda, Phys. Rev. Lett. **103**, 085301 (2009).
15. K. Masuda, T. Hatsuda, T. Takatsuka, Astrophys. J. **764**, 12 (2013) arXiv:1205.3621 [nucl-th].
16. K. Masuda, T. Hatsuda, T. Takatsuka, PTEP **2013**, 073D01 (2013) arXiv:1212.6803 [nucl-th].
17. K. Masuda, T. Hatsuda, T. Takatsuka, PTEP **2016**, 021D01 (2016) arXiv:1506.000984 [nucl-th].
18. D.E. Alvarez-Castillo, S. Benic, D. Blaschke, R. Lastowiecki, Acta Phys. Pol. Suppl. **7**, 203 (2014) arXiv:1311.5112 [nucl-th].
19. T. Hell, W. Weise, Phys. Rev. C **90**, 045801 (2014) arXiv:1402.4098 [nucl-th].
20. T. Kojo, P.D. Powell, Y. Song, G. Baym, Phys. Rev. D **91**, 045003 (2015) arXiv:1412.1108 [hep-ph].
21. T. Nagae, Prog. Theor. Phys. Suppl. **185**, 299 (2010).
22. H. Tamura, Prog. Theor. Phys. Suppl. **185**, 315 (2010).
23. K. Nakazawa, H. Takahashi, Prog. Theor. Phys. Suppl. **185**, 335 (2010).
24. HAL QCD Collaboration (T. Inoue *et al.*), Nucl. Phys. A **881**, 28 (2012).
25. T. Takatsuka, Prog. Theor. Phys. Suppl. **156**, 84 (2004) and references therein.
26. I. Vidana, AIP Conf. Proc. **1645**, 79 (2015).
27. S. Nishizaki, Y. Yamamoto, T. Takatsuka, Prog. Theor. Phys. **105**, 607 (2001).
28. S. Nishizaki, Y. Yamamoto, T. Takatsuka, Prog. Theor. Phys. **108**, 703 (2002).
29. T. Takatsuka, S. Nishizaki, R. Tamagaki, AIP Conf. Proc. **1011**, 209 (2008).
30. Y. Yamamoto, T. Furumoto, N. Yasutake, T.A. Rijken, Phys. Rev. C **90**, 045805 (2014) arXiv:1406.4332 [nucl-th].
31. D. Lonardoni, A. Lovato, S. Gandolfi, F. Pederiva, Phys. Rev. Lett. **114**, 092301 (2015) arXiv:1407.4448 [nucl-th].
32. T. Katayama, K. Saito, Phys. Lett. B **747**, 43 (2015) arXiv:1501.05419 [nucl-th].
33. M. Baldo, G.F. Burgio, H.J. Schulze, Phys. Rev. C **61**, 055801 (2000).
34. K. Tsubakihara, H. Maekawa, H. Matsumiya, A. Ohnishi, Phys. Rev. C **81**, 065206 (2010).
35. A. Akmal, V.R. Pandharipande, D.G. Ravenhall, Phys. Rev. C **58**, 1804 (1998).
36. T. Takatsuka, S. Nishizaki, Y. Yamamoto, R. Tamagaki, Prog. Theor. Phys. **115**, 355 (2006) nucl-th/0601043.
37. B. Friedman, V.R. Pandharipande, Nucl. Phys. A **361**, 502 (1981).
38. A.D. Linde, Phys. Lett. B **96**, 289 (1980).
39. T. Hatsuda, T. Kunihiro, Phys. Rev. Lett. **55**, 158 (1985).
40. C.E. DeTar, Phys. Rev. D **32**, 276 (1985).
41. T. Hatsuda, T. Kunihiro, Phys. Rep. **247**, 221 (1994).
42. M. Buballa, Phys. Rept. **407**, 205 (2005).
43. M. Kobayashi, T. Maskawa, Prog. Theor. Phys. **44**, 1422 (1970).
44. G. 't Hooft, Phys. Rev. D **14**, 3432 (1976) **18**, 2199(E) (1978).
45. N.M. Bratovic, T. Hatsuda, W. Weise, Phys. Lett. B **719**, 131 (2013) arXiv:1204.3788 [hep-ph].
46. O. Lourenco, M. Dutra, T. Frederico, A. Delfino, M. Malheiro, Phys. Rev. D **85**, 097504 (2012).
47. T. Hatsuda, M. Tachibana, N. Yamamoto, G. Baym, Phys. Rev. Lett. **97**, 122001 (2006).
48. N. Yamamoto, M. Tachibana, T. Hatsuda, G. Baym, Phys. Rev. D **76**, 074001 (2007).
49. H. Abuki, G. Baym, T. Hatsuda, N. Yamamoto, Phys. Rev. D **81**, 125010 (2010).
50. J.P. Blaizot, J.Y. Ollitrault, Phys. Lett. B **191**, 21 (1987).
51. M. Asakawa, T. Hatsuda, Phys. Rev. D **55**, 4488 (1997).
52. A.W. Steiner, J.M. Lattimer, E.F. Brown, Astrophys. J. **765**, L5 (2013) arXiv:1205.6871 [nucl-th].
53. F. Ozel, D. Psaltis, T. Guver, G. Baym, C. Heinke, S. Guillot, arXiv:1505.05155 [astro-ph.HE].
54. M. Alford, M. Braby, M.W. Paris, S. Reddy, Astrophys. J. **629**, 969 (2005) nucl-th/0411016.
55. R. Lastowiecki, D. Blaschke, T. Fischer, T. Klahn, arXiv:1503.04832 [nucl-th].
56. M. Prakash, J.M. Lattimer, J.A. Pons, A.W. Steiner, S. Reddy, Lect. Notes Phys. **578**, 364 (2001) astro-ph/0012136.

57. H.T. Janka, Annu. Rev. Nucl. Part. Sci. **62**, 407 (2012) arXiv:1206.2503 [astro-ph.SR].
58. L.F. Roberts, Astrophys. J. **755**, 126 (2012) arXiv:1205.3228 [astro-ph.HE].
59. M. Prakash, J.R. Cooke, J.M. Lattimer, Phys. Rev. D **52**, 661 (1995).
60. K. Nakazato, K. Sumiyoshi, S. Yamada, Phys. Rev. D **77**, 103006 (2008) arXiv:0804.0661 [astro-ph].
61. G. Pagliara, M. Hempel, J. Schaffner-Bielich, Phys. Rev. Lett **103**, 171102 (2009) arXiv:0907.3075 [astro-ph.HE].
62. H. Chen, G.F. Burgio, H.J. Schulze, N. Yasutake, Astron. Astrophys. **551**, A13 (2013) arXiv:1302.6074 [astro-ph.SR].
63. M. Hempel, J. Schaffner-Bielich, Nucl. Phys. A **837**, 210 (2010) arXiv:0911.4073 [nucl-th].
64. N. Buyukcizmeci, A.S. Botvina, I.N. Mishustin, R. Ogul, M. Hempel, J. Schaffner-Bielich, F.-K. Thielemann, S. Furusawa *et al.*, Nucl. Phys. A **907**, 13 (2013) arXiv:1211.5990 [nucl-th].
65. G. Baym, C. Pethick, P. Sutherland, Astrophys. J. **170**, 299 (1971).
66. T. Takatsuka, S. Nishizaki, J. Hiura, Prog. Theor. Phys. **92**, 779 (1994).
67. T. Takatsuka, Prog. Theor. Phys. **95**, 901 (1996).
68. K. Hotokezaka, K. Kiuchi, K. Kyutoku, T. Muranushi, Y. Sekiguchi, M. Shibata, K. Taniguchi, Phys. Rev. D **88**, 044026 (2013) arXiv:1307.5888 [astro-ph.HE].
69. K. Hotokezaka, K. Kyutoku, M. Shibata, Phys. Rev. D **87**, 044001 (2013) arXiv:1301.3555 [gr-qc].
70. K. Hotokezaka, K. Kyutoku, H. Okawa, M. Shibata, Phys. Rev. D **91**, 064060 (2015) arXiv:1502.03457 [gr-qc].